Solution Structure of the Actinorhodin Polyketide Synthase Acyl Carrier Protein from *Streptomyces coelicolor* A3(2)[†,‡]

Matthew P. Crump,[§] John Crosby,[§] Christopher E. Dempsey,[||] John A. Parkinson,[⊥] Martin Murray,[§] David A. Hopwood,[#] and Thomas J. Simpson*[,§]

School of Chemistry, University of Bristol Molecular Recognition Centre, University of Bristol, Cantock's Close, Bristol BS8 1TS, U.K., Department of Biochemistry, University of Bristol Molecular Recognition Centre, University of Bristol, University Walk, Bristol BS8 1TD, U.K., Department of Chemistry, Ultra High Field NMR Centre, University of Edinburgh, King's Buildings, West Mains Road, Edinburgh EH9 3JJ, U.K., and John Innes Centre, Norwich NR4 7UH, U.K.

Received January 2, 1997[⊗]

ABSTRACT: The solution structure of the actinorhodin acyl carrier protein (*act apo*-ACP) from the polyketide synthase (PKS) of *Streptomyces coelicolor* A3(2) has been determined using ^{1}H NMR spectroscopy, representing the first polyketide synthase component for which detailed structural information has been obtained. Twenty-four structures were generated by simulated annealing, employing 699 distance restraints and 94 dihedral angle restraints. The structure is composed, principally, of three major helices (1, 2, and 4), a shorter helix (3) and a large loop region separating helices 1 and 2. The structure is well-defined, except for a portion of the loop region (residues 18−29), the N-terminus (1−4), and a short stretch (57−61) in the loop connecting helices 2 and 3. The RMS distribution of the 24 structures about the average structure is 1.47 Å for backbone atoms, 1.84 Å for all heavy atoms (residues 5−86), and 1.01 Å for backbone atoms over the helical regions (5−18, 41−86). The tertiary fold of *act apo*-ACP shows a strong structural homology with *Escherichia coli* fatty acid synthase (FAS) ACP, though some structural differences exist. First, there is no evidence that *act apo*-ACP is conformationally averaged between two or more states as observed in *E. coli* FAS ACP. Second, *act apo*-ACP shows a disordered N-terminus (residues 1−4) and a longer flexible loop (19−41 with 19−29 disordered) as opposed to *E. coli* FAS ACP where the N-terminal helix starts at residue 3 and the loop region is three amino acids shorter (16−35). Most importantly, however, although the *act apo*-ACP structure contains a hydrophobic core, there are in addition a number of buried hydrophilic groups, principally Arg72 and Asn79, both of which are 100% conserved in the PKS ACPs and not the FAS ACPs and may therefore play a role in stabilizing the growing polyketide chain. The structure−function relationship of *act* ACP is discussed in the light of these structural data and recent genetic advances in the field.

Polyketides are a diverse family of metabolites produced by organisms ranging from filamentous bacteria (actinomycetes) and fungi to higher plants (O'Hagan, 1991, 1995; Simpson, 1995). Their widespread occurrence and structural diversity are matched by a range of biological properties from antibiosis to immunosuppression and metabolic regulation. The polyketides are related by a common biosynthetic origin in which the carbon skeleton is assembled from the sequential condensation of short-chain carboxylic acids such as acetate, propionate, or butyrate. The assembly is catalyzed by the polyketide synthases (PKSs),[1] large multifunctional enzymes which are conceptually similar to the fatty acid synthases (FASs) (Hopwood & Sherman, 1990; Robinson, 1991; Hopwood & Khosla 1992). Following each condensation, FASs typically complete a full reductive cycle of ketoreduction, dehydration, and enoyl reduction, while the PKSs can be more specific by curtailing or omitting many of these steps. The "programming" involved in choosing where to complete or curtail a cycle involves a complex series of choices rising to 4^n (n is the number of condensations); a major challenge in the field has been to elucidate how this is achieved in such a diverse set of organisms.

The PKSs responsible for biosynthesis of aromatic polyketide antibiotics in streptomycetes (Figure 1) resemble the type II FAS of *Escherichia coli*, with separate enzymes for each subreaction of carbon chain assembly and modification and with all sites being used repeatedly at each relevant step. For these systems, the work of Khosla et al., Fu et al., and MacDaniel et al. has provided information about the "programmed" assembly of aromatic polyketides from streptomycetes (Khosla et al., 1992, 1993; McDaniel et al., 1993a,b, 1994a,b, 1995a,b; Fu et al., 1994a,b). In *Streptomyces coelicolor* the genes responsible for actinorhodin

[†] This work was funded by the Engineering and Physical Sciences (EPSRC) and Biotechnology and Biological Sciences (BBSRC) Research Councils, the Leverhulme Trust, the John Innes Foundation, and the Wellcome Trust.

[‡] Coordinates have been deposited in the Brookhaven Protein Data Bank (accession code BNL-4765).

* Author to whom correspondence should be addressed. Tel: (44) 117 9287656. Fax: (44) 117 9298611.

[§] School of Chemistry, University of Bristol.

[||] Department of Biochemistry, University of Bristol.

[⊥] University of Edinburgh.

[#] John Innes Centre.

[⊗] Abstract published in *Advance ACS Abstracts,* May 1, 1997.

[1] Abbreviations: ACP, acyl carrier protein; *act*, actinorhodin; ASA, accessible surface area; NMR, nuclear magnetic resonance; NOE, nuclear Overhauser effect; 1D, one dimensional; 2D, two dimensional; NOESY, 2D NOE spectroscopy; DQF-COSY, double-quantum-filtered correlated spectroscopy; TOCSY, total correlation spectroscopy; PKS, polyketide synthase; FAS, fatty acid synthase; *S. griseus*, *Streptomyces griseus*; Tris, tris(hydroxymethyl)aminomethane.

S0006-2960(97)00006-8 CCC: $14.00

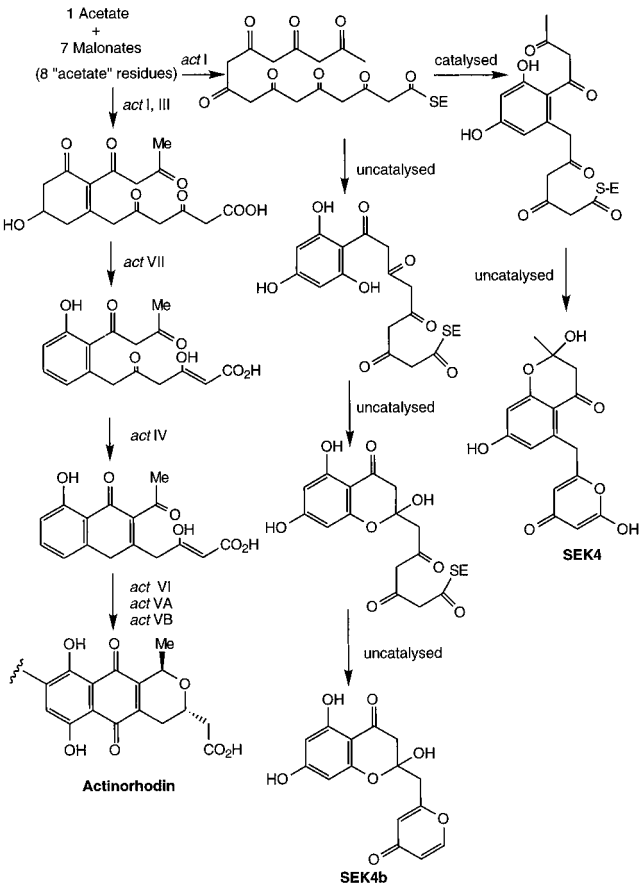

FIGURE 1: Proposed biosynthetic pathway to actinorhodin and the products SEK4 and SEK4b produced by the minimal PKS. Abbreviations: *act* I, minimal PKS comprising ORF1 + ORF2, condensing enzyme/acyl transferase + chain length determining factor, and ORF3, acyl carrier protein (McDaniel et al., 1994b); *act* III, ketoreductase (Hallam et al., 1988; Fu et al., 1994a); *act* VII, putative aromatase, and *act* IV, cyclase (McDaniel et al., 1994a); *act* VI, *act* VA, *act* VB, hydroxylase(s), oxidoreductases, and dimerase (Fernández-Moreno et al., 1994; Kendrew et al., 1995).

production are clustered and are thought to encode 22 proteins (Fernández-Moreno et al., 1994), most of which are involved in regulation, actinorhodin export, and tailoring of the assembled polyketide chain (i.e., cyclase, hydroxylase and dimerase enzymes). The assembly of "minimal PKS" sets has shown, however, that just three of these genes (*act* I-ORF 1, -ORF 2, and -ORF 3) encoding an acyl carrier protein (ORF 3), ketosynthase (ORF 1), and a "chain length determining factor" (ORF 2) are sufficient to produce a polyketide chain of the correct length and cyclize it to an initial intermediate containing a single resorcinol-type ring (Figure 1). The completion of this process effectively ends classical polyketide biosynthesis. Following these steps, further enzymes downstream tailor the polyketide chain to produce actinorhodin (Figure 1). More recently it has been shown that the *act* minimal PKS, comprising only *act* I-ORFs 1−3, produces two compounds, SEK4, and an incorrectly cyclized compound, SEK4b (Fu et al., 1994b) (Figure 1). It appears that SEK4b could arise from an unusual, nonenzyme-mediated cyclization beginning at the methyl end of the polyketide, in turn suggesting premature exposure of this region to the surrounding medium. These results highlight the fact that the minimal PKS alone cannot fully control the initial biosynthetic steps and that noncovalent interactions between the ACP, polyketide, the three minimal PKS subunits, and other downstream enzymes (in this case the ketoreductase) may be required for full stereochemical control.

To understand how the initial biosynthetic control is exerted requires a knowledge of the 3D structures and of the interaction between the ACP, the polyketide assembly intermediates, and the enzymes with which they interact. At present, however, the structural and biochemical characterization of the type II polyketide synthases is not well developed. The ACPs of the type II polyketide synthases responsible for the biosynthesis of tetracenomycin (Shen et al., 1992), actinorhodin, frenolicin, granaticin, and oxytetracycline (Crosby et al., 1995) have been characterized and isolated in sufficient quantities for NMR study. The acyl carrier proteins from these enzyme complexes are small acidic proteins bearing a 4′-phosphopantetheine group that provides a free thiol to which a growing polyketide or fatty acid is attached via a thioester linkage (Prescott & Vagelos, 1972). Genetic substitution experiments have shown the presence of ACP to be essential for function of the PKS but also that alternative polyketide synthase ACPs (and even a putative fatty acid synthase ACP) may be substituted to produce an apparently functional PKS (Khosla et al., 1992, 1993).

We have previously shown that the *act* ACP is a four-helix bundle with a strong secondary structure homology with the *E. coli* FAS ACP (sequence similarity 47%; Crump et al., 1996). To help to determine the ACP's role as a carrier of the growing, inherently unstable polyketide chain, we have solved by NMR the solution structure of *act apo*-ACP, which represents the first three-dimensional structure of any PKS component. We discuss the structural features in relation to the FAS *E. coli* ACP and the structure−function relationships of *act* ACP in polyketide biosynthesis.

MATERIALS AND METHODS

Sample Preparation. The details of the NMR sample preparation have been reported previously (Crosby et al., 1995; Crump et al., 1996). ACP selectively labeled with (2*S*,4*R*)-[5,5,5-$^2H_3$]leucine was prepared as follows. A sterile seed flask containing 100 mL of LB medium [with 100 μL each of ampicillin (50 mg/L) and kanamycin (50 mg/L)] was used to inoculate 25 500 mL flasks, each containing 100 mL of LB media. The cultures were allowed to grow to an A_{595nm} of 1.5. The bacteria were removed by centrifugation (7000 rpm, 15 °C, 15 min) and washed with 100 mL of M9 minimal media. The pellet was resuspended in 50 mL of M9 media supplemented with 0.01% (w/v) of each amino acid (including (2*S*,4*R*)-[5,5,5-$^2H_3$]leucine), and 2 mL of this solution was used to inoculate each 500 mL flask containing 100 mL of M9 minimal media and antibiotics. The bacteria were induced immediately by raising the temperature to 42 °C and then left to grow for a further 18 h at 30 °C before harvesting. The protein was purified as described previously and characterized by electrospray mass spectrometry (ESMS) (Crosby et al., 1995).

NMR Spectroscopy. NMR experiments were performed on a Jeol Alpha 500 MHz spectrometer. All spectra were acquired in phase-sensitive mode employing quadrature detection in both dimensions using the method of States et al. (1982) and with presaturation of the water signal using a DANTE pulse train (Morris & Freeman, 1978). The

following two-dimensional experiments were performed: NOESY (Jeener et al., 1979; Wider et al., 1984), with mixing times of 75, 100, and 150 ms; TOCSY (Braunschweiler & Ernst, 1983; Bax & Davis, 1985) with mixing times of 75 and 100 ms; and DQF-COSY (Rance et al., 1983). Data sets were collected with 2048 real points in the t_2 dimension with 256 or 512 t_1 increments and at temperatures of 25 and 40 °C to help resolve assignment difficulties associated with spectral crowding. Several spectra were acquired at a proton resonance frequency of 600 MHz on a Varian 600 MHz spectrometer at the Department of Chemistry, University of Edinburgh. DQF-COSY, NOESY with a mixing time of 150 ms, and TOCSY spectra with a mixing time of 65 ms were acquired with improved resolution and sensitivity, aiding subsequent assignments in many cases.

For the characterization of slow amide exchange, NOESY spectra were recorded at 500 MHz for 4, 8, 12, 24, and 72 h after the protein was dissolved in D_2O (99.90%).

The intensities of the NOE peaks from a 75 and 150 ms NOESY experiment were examined and the cross peaks classified as strong, medium, weak, and very weak. The cross peaks were converted to interproton distances ranging between 1.8−2.8 Å (strong), 1.8−3.3 Å (medium), 1.8−4.0 Å (weak), and 1.8−5.0 Å (very weak). For partially resolved peaks, volume integration was approximated by taking row and column integrals and evaluating with the formula (Holak et al., 1987)

$$V = \sum_j I(j_0)I(i_0)/Hi_0j_0 \qquad (1)$$

where $I(j_0)$ is the 1D integral taken along f_2, $I(i_0)$ is the 1D integral taken along f_1 and Hi_0j_0 is the intensity of the cross peak at its center.

Backbone dihedral angles were calculated from coupling constants measured in a DQF-COSY experiment zero-filled to 8K points in the f_2 dimension. For $^3J_{HNH\alpha} < 5$ Hz the backbone ϕ angle was restrained to $-60° \pm 30°$, and for $^3J_{HNH\alpha} \geq 9$ Hz the ϕ angle was restrained to $120° \pm 30°$. No ψ angles were included. To determine the χ^1 angles, a PE-COSY (Mueller, 1987) data set was acquired at 25 °C, and the CαH−CβH coupling constants were extracted from the simple multiple patterns. In the analysis, it was assumed that the amino acid side chains adopt one of three energetically favorable staggered conformations with $\chi^1 = +60°$, 180°, or −60°. The side chains analyzed were restricted to a staggered conformation only if the measured coupling constants were completely consistent with the intraresidue NH−CβH and CαH−CβH NOE obtained in a 75 ms NOESY data set.

To obtain stereospecific assignments for several of the diastereotopic pairs of leucine methyls, the upfield regions of the DQF-COSY of the unlabeled and (2*S*,4*R*)-[5,5,5-$^2H_3$]leucine-labeled *act apo*-ACP were compared. A comparison of the spectra revealed a missing δCH_3 peak for leucines 4, 5, 10, 14, 26, 31, 45, 52, and 75 in the spectrum of the labeled ACP.

Experimental constraints for hydrogen bonds within α-helices were added after the initial set of simulated annealing structures was calculated. A total of 36 restraints for 18 α-helical backbone hydrogen bonds were included [CO−NH(i,$i+4$) = 1.8−2.3 Å, CO−N(i,$i+4$) = 2.7−3.2 Å]. A single constraint was added for the hydrogen bond between Leu5 NH and the γO of Asn79 which was identified after the first round of calculations.

Calculations were performed using the program X-PLOR 3.1 (Brünger et al., 1987) and the dynamic simulated annealing protocol for extended-strand starting structures (Nilges et al., 1988). The initial structure was energy minimized to provide an energetically feasible starting structure with 2000 cycles of Powell energy minimization. High temperature dynamics were run for 30 ps at an initial temperature of 1000 K, with each of the calculations initiated using randomized dynamics trajectories. Throughout the entire calculation, after each time step, bond lengths and angles were corrected to a fixed length [SHAKE (Ryckaert et al., 1977)]. A total of 699 NOE distance restraints and 94 dihedral angle constraints were used in the calculations. A low slope (asymptote = 0.1) of the NOE term (a soft square well potential, r_{switch} 0.5 Å) was used through the initial stage, and a force constant, k_{NOE}, for the experimental NOE distance restraints of 50.0 kcal/(mol Å^2) was employed. Geometric center averaging was used for ambiguous assignments, e.g., methylene protons or methyl groups, and pseudoatoms were employed (Wüthrich et al., 1983) with the appropriate upper bound corrections on the experimental restraints. Long-range contacts involving ambiguous aromatic ring proton assignments (due to fast ring flipping) were modeled with (r^{-6}) NOE averaging. In the next stage, the slope of the asymptote was increased to 1.0 for the final 10 ps of high temperature dynamics. The system was then slowly cooled (annealed) to a temperature of 300 K in 50 K steps over a period of 20 ps. The nonbonded repulsive term was increased concomitantly with the NOE asymptote in an exponential fashion to prevent further crossing of atoms during annealing. At 300 K, a final stage of 400 steps of Powell minimization was performed to yield the final simulated annealing structures. All of the simulations were carried out in the absence of internally bound water molecules, or surrounding solvent molecules, and the electrostatic contributions from Arg, Glu, and Asp residues were not included. Each structure was analyzed for NOE and dihedral angle restraint violations, and visualizsation of structures with Insight II (Biosym) allowed populations of similar conformers to be superimposed. Within the 30 structures generated by the simulated annealing (SHAKE) protocol, 24 had a global fold with consistently superimposable regions of regular structure and significantly lower energy terms. Visualization of structures within Insight II allowed hydrogen-bonding interactions to be assessed and compared to amide exchange data. With the addition of hydrogen bond restraints, these structures were further refined with high temperature dynamics at 1000 K and cooling of the system in slow 25 K steps to a final 300 K over a period of 30 ps to give the final family of 24 structures.

RESULTS

(a) NMR Restraints. A total of 699 NOE distance restraints were obtained from the NOESY spectra and were used in the final structure calculations. These were distributed as 240 intraresidue restraints, 235 sequential restraints, 131 short-range restraints, and 93 long-range restraints. In addition, a total of 63 ϕ , 29 χ^1 and 2 χ^2 angles were included in the structure calculations. The distribution of NOEs is shown in Figure 2. Labeling of the leucines with (2*S*,4*R*)-[5,5,5-$^2H_3$]leucine allowed stereospecific assignments to be

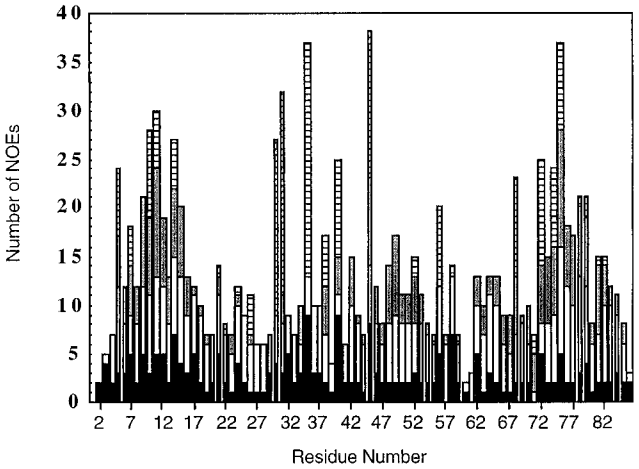

FIGURE 2: Summary of the number and nature of the NOE constraints per residue versus the amino acid number. The NOEs are represented as follows: intraresidue (black), sequential (open), short range (stippled), and long range (horizontally hatched).

made for Leu4 (0.97^R, 0.90^S), Leu5 (0.70^R, 0.68^S), Leu10 (1.04^R, 1.15^S), Leu14 (0.77^R, 0.93^S), Leu26 (0.73^R, 0.84^S), Leu31 (0.81^R, 0.49^S), Leu52 (0.89^R, 1.06^S), Leu45 (0.38^R, 0.28^S), and Leu75 (0.82^R, 0.90^S). This allowed a greater number of restraints to be included which required no center-averaged pseudoatom correction.

(b) Quality of the Calculated Structures. A total of 30 structures were calculated of which 24 displayed a similar global fold consisting of a four-helix bundle with no NOE violations >0.5 Å. Hydrogen bond constraints were added, and a further run of dynamics was applied as discussed in Materials and Methods. The final set of 24 structures (referred to collectively as ⟨ACT⟩) was obtained, having discarded six structures because of misfolding and higher residual NOE energies. Structural statistics for the final 24 structures are shown in Table 1. The average structure $\overline{\text{ACT}}$ was calculated from the mean coordinates of the set of 24 structures, and $\overline{\text{ACT}}_r$ is the final structure obtained by restrained minimization (4000 steps) to remove poor covalent geometry and nonbonded contacts. The final minimized structure shows no NOE violations >0.3 Å, no angle violations >3°, and possesses good covalent geometry and nonbonded contacts as evidenced by small values for the van der Waals energy (E_{VDW}).

A best fit superposition of the 24 structures with $\overline{\text{ACT}}_r$ is shown in Figure 3. Figure 4 shows the RMSDs by residue for ⟨ACT⟩ vs the averaged structure. Plots for both the backbone deviations (Figure 4A) and all non-hydrogen atoms are shown (Figure 4B). There is a clear correlation between the regions of well-defined structure, principally helices 1 and 4 and the structured region of the loop from residues 30 to 41, and the number of NMR restraints per residue over these regions. High RMSDs are observed over the first four residues at the N-terminus (2−8 Å), and in the first loop region between residues 18 and 29, all of which show no long-range NOEs. The atomic RMSDs for the 24 structures (residues 5−86) superimposed on the geometric average structure $\overline{\text{ACT}}$ are 1.47 Å for the backbone atoms and 1.84 Å for all heavy atoms. With superpositions over residues 5−18 and 41−86 (i.e., principally the four helices and the loop connecting helices 2 and 3), this number drops to 1.01 Å for backbone atoms and 1.45 Å for all atoms. If residues 5−18 and 68−86 are fitted to the geometric average, the backbone atoms show an average RMSD of 0.57 and 1.02 Å for all atoms. The backbone is, therefore, well-defined for the helical regions, especially helices 1 and 4, for which there is good definition over the side chains as well. Residues 19−29 appear to adopt an apparently random conformation relative to the well-defined orientation of the four helices.

Table 1: Structural Statistics and Atomic RMS Differences for *act apo*-ACP

	⟨ACT⟩[a]	$\overline{\text{ACT}}_r$
RMS deviation from exptl restraints (Å)		
long ($\|i-j\|>5$)[b]	0.019 ± 0.010	0.001
short ($1\le\|i-j\|\le 5$)	0.018 ± 0.009	0.005
sequential ($\|i-j\|=1$)	0.022 ± 0.007	0.008
interresidue (R^{-6} averaged) long	0.023 ± 0.004	0.001
intraresidue (center averaged)	0.008 ± 0.003	0.004
E_{NOE} (kcal mol^{-1})[c]	10.03 ± 4.0	1.07
E_{DIHE} (kcal mol^{-1})	0.204 ± 0.15	0.086
E_{VDW} (kcal mol^{-1})	0.014 ± 0.319	0.200
deviations from idealized geometry[d]		
bonds (Å)	0.003 ± 0.0003	0.0007
angles (deg)	0.460 ± 0.024	0.34
impropers (deg)	0.265 ± 0.014	0.213

[a] The structural notation is as follows: ⟨ACT⟩ is the final 24 simulated annealing structures; $\overline{\text{ACT}}$ is the mean structure obtained by averaging the coordinates of each ACT structure best fitted over residues 5−86; $\overline{\text{ACT}}_r$ is the structure obtained after 4000 steps of restrained energy minimization of $\overline{\text{ACT}}$. [b] The RMS deviation of the experimental restraints is calculated with respect to the upper and lower limits of the input restraints. [c] The values for E_{NOE} are calculated from a square well potential with a force constant of 50 kcal mol^{-1} rad^{-2}. E_{VDW} is calculated with a force constant of 4 kcal mol^{-1} Å^{-4}, and the final van der Waals radii were set to 0.75 times the value used in the standard CHARMM force field. [d] The values for bonds, angles, and impropers show the deviation from ideal values based on perfect stereochemistry.

The precision of the torsion angles is assessed in terms of the order parameter S (Hyberts et al., 1992; Pallaghy et al., 1993). The angular order parameter is a statistical parameter where $S = 1$ if a given torsion angle is identical in every member of a structure family and $S = 0$ if it appears completely undefined. Typically, S values of 1.00, 0.99, 0.98, and 0.90 correspond to angular standard deviations of 0°, 8°, 18°, and 26°, respectively. In all, 76% of the residues have $S(\phi) > 0.90$ (not including Met1 and Ala2) (Figure 4C), and 71% of residues have $S(\psi) > 0.90$ (Figure 4D), indicating that a large proportion of the torsion angles was well-defined. The exceptions to this lie in a segment of the first loop (residues 19−29) between helices 1 and 2 and the short second loop connecting helices 2 and 3. In particular, residues Gly19, Glu20, Gly23, Thr24, Gly28, and Asp29 all show either $S(\phi)$ or $S(\psi)$ less than 0.5. Examination of the structures shows that the backbone definition is very low over this region and there are few NOEs for these residues. Since the chemical shift dispersion was good for the NOESY spectra, a lack of restraints is unlikely to be due to fortuitous overlaps of NOE signals but rather indicates real flexibility for residues in this region. The majority of the residues from 19 to 29 (>90%) are polar, acidic, or glycines, suggesting that this region is highly solvent exposed with few residues available for hydrophobic packing within the protein core. Examination of spectra after short periods of hydrogen exchange (<4 h) revealed no stable amides within this region, further indicating a lack of stable secondary or tertiary

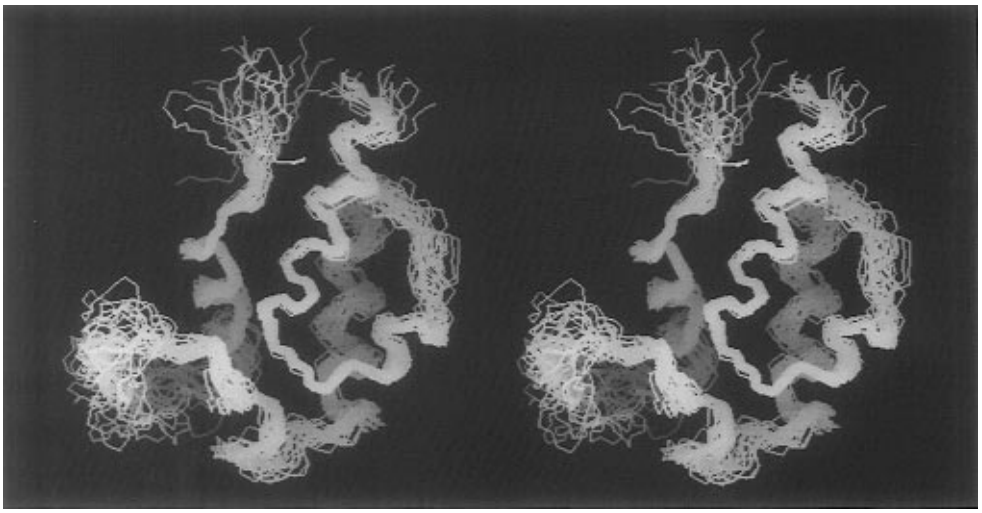

FIGURE 3: Stereoview showing the best fit superposition of the backbone (N, C^{α}, C) atoms of the 24 simulated annealing structures. All the residues are shown (1−86), and the best fit was taken over residues 5−18 and 30−86.

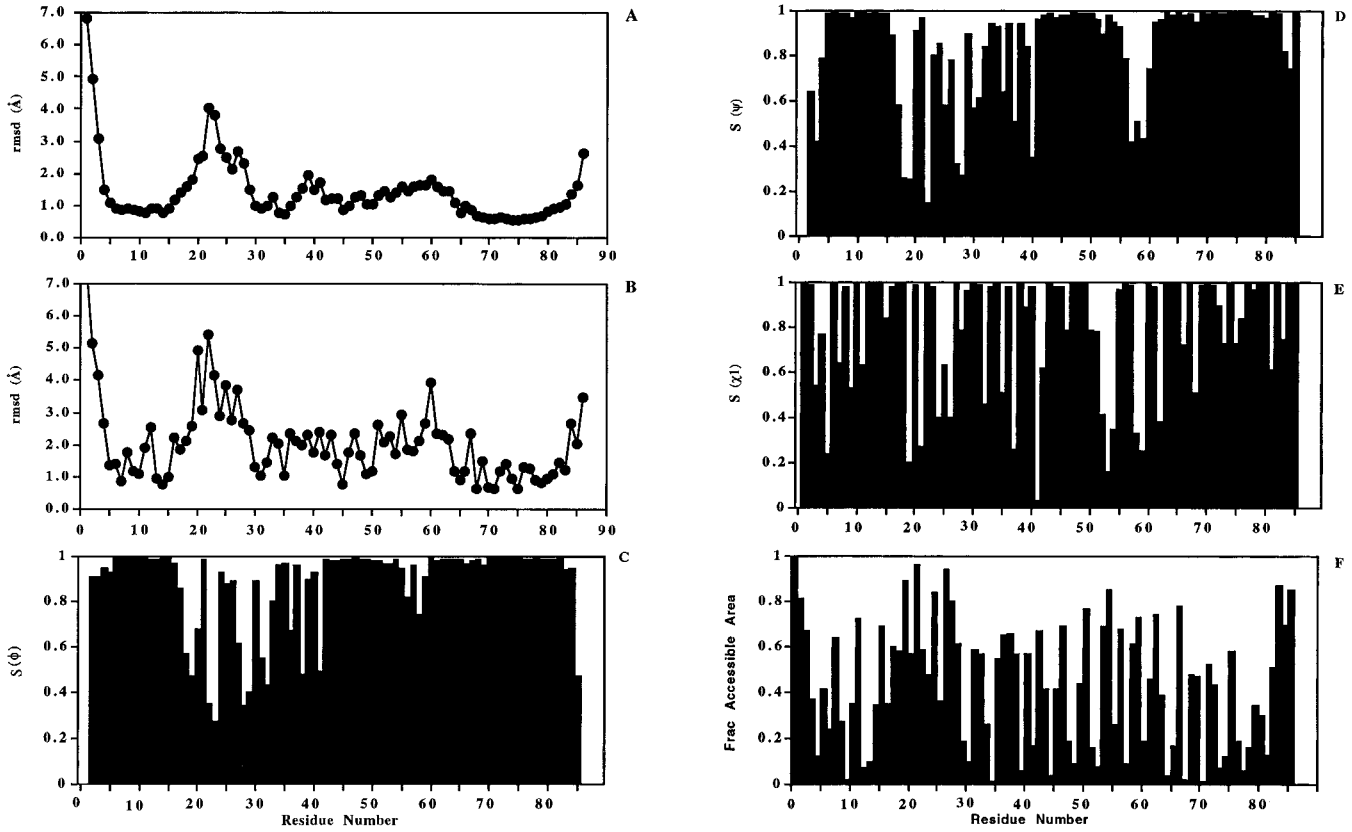

FIGURE 4: Atomic RMS distribution of the 24 individual simulated annealing structures about the average structure best fitted for residues 5−86, for backbone atoms only (A) and for all heavy atoms (B). Angular order parameters are shown for ϕ (C), ψ (D), and χ^1 (E). Also shown is the fractional solvent-accessible area calculated for the average minimized structures (F).

structure. For the protein as a whole, 47% of the side chains have $S(\chi^1) > 0.90$ (not including alanines and glycines) (Figure 4E). $S(\chi^1) < 0.65$ is observed for charged residues such as Asp (22, 25), Glu (20, 53), Arg (55), Ser (27, 54, 59), and several residues (Leu4, Thr6) at the N-terminus. These residues are generally located at the surface of the protein as evidenced by calculated fraction-accessible surface area (frac ASA) (Figure 4F) (Lee & Richards, 1971).

The local angle geometry of the 24 structures was analyzed by Procheck−NMR (MacArthur & Thornton, 1993) for the three main chain angles ϕ, ψ, and χ^1. A Ramachandran plot showed that 71% of all the residues analyzed have (ϕ,ψ) angles that lie in the most favored regions and 26% lie in the additionally allowed regions. Those residues that lie in the generously allowed regions and forbidden regions in some models (2% and 1%, respectively) are predominantly residues with very few NMR restraints (i.e., Ala2, Thr3, Leu4 at the N-terminus of helix 1; Glu20, Thr21, Thr 24, Asp25, Leu26, Ser27 in the largely unstructured portion of the loop between helices 1 and 2; Ser42 at the N-terminus of helix 2 and Ser59 in the loop between helices 2 and 3). There is no NMR evidence to suggest that these really do have positive angles, and no dihedral restraints were invoked for these because they all show averaged $^3J_{HN\alpha}$ coupling

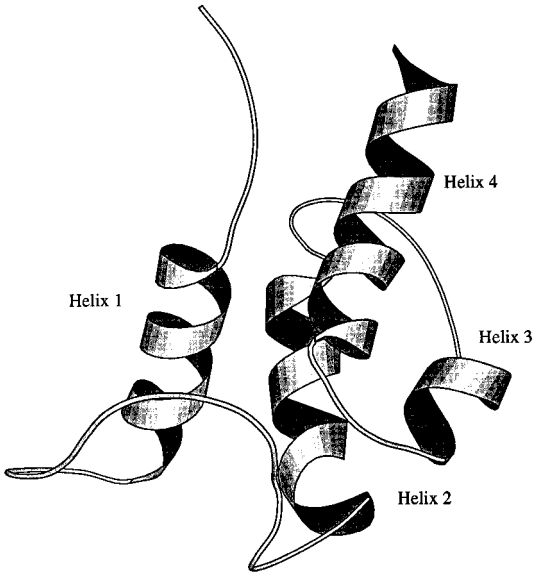

FIGURE 5: Schematic diagram showing the restrained minimized average structure of *act apo*-ACP. The figure was created using the program Molscript (Kraulis, 1991).

constants of 6−8 Hz. A single Ramachandran plot generated for the averaged, minimized structure $\overline{ACT}_r$ shows 73.3% of the ϕ/ψ angles in the most favored regions, 25.3% in the additionally allowed regions, 1.3% in generously allowed regions, and no residues in forbidden areas. For the more highly structured regions over residues 5−18, 30−58, and 62−85, these figures are 82.1%, 16.1%, 1.8%, and 0%, respectively.

(c) Hydrogen Bonds. The structure of *act* ACP is characterized by a number of long-range hydrogen bonds in addition to the short-range bonds reported previously for the secondary structure (Crump et al., 1996). A total of 24 slowly exchanging amides were identified of which 18 are involved in helical hydrogen bonds (helix 1, amide NH of residues 10−15 inclusive; helix 2, amide NH of residues 49−53 inclusive; helix 4, amide NH of residues 73−79 inclusive). The remaining six, the amide protons of Leu5, Leu33, Arg34, Ile38, Val68, and Thr70, are involved in hydrogen bonds within turns or the tertiary structure of the protein and possess exchange protection factors (Bai et al., 1993) of at least 200-fold. In the structures generated from the first round of simulated annealing, four of the hydrogen-bonding partners could be identified from visualization of the structures. These included Leu5(NH) to Asn79(γCO), Ile38(NH) to Arg34(CO), Val68(NH) to Ala65(CO), and Thr70(NH) to Thr70(γO).

Five potential short- and long-range hydrogen bonds could be identified by inspection of the structures, although for those involving backbone amide NHs, no significant exchange protection was found. These included the long-range hydrogen bonds Tyr56(ϵOH) to Asp9(γOC), Thr7(γO) to Arg72(ζNH_2), Arg67(NH) to Asp63(CO), Gly66(NH) to Asp62(CO), and Ala65(NH) to Pro61(CO).

(d) Description of the Structure. The average minimized structure of *act apo*-ACP is shown as a Molscript schematic in Figure 5. The structure consists of three major α-helices (1, 7−16; 2, 42−53; and 4, 72−85), a shorter helix (3, 62−67), a large first loop separating helices 1 and 2, and a shorter second loop connecting helices 2 and 3. Helices 1 and 4 run antiparallel and are particularly well-defined by numerous

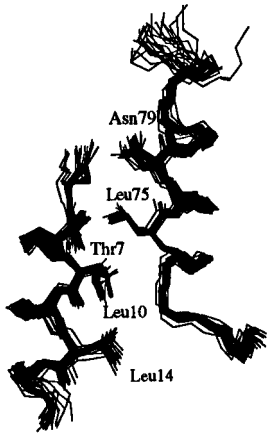

FIGURE 6: The best fit superpositions of residues 7−18 and 68−86 (helices 1 and 4) and selected buried side chains for the 24 simulated annealing structures.

contacts between Leu5, Thr7, Leu10, Leu75, and Asn79 (Figure 6). The backbone atomic coordinates for helix 2, which runs almost parallel to helix 4, appears slightly less well-defined in the final structure, and its orientation is principally defined by the long-range interactions of Leu52 and Leu45. The four helices are amphipathic, with the notable exceptions of Arg72 and Asn79 (frac ASA 0.52 and 0.16), which are buried, and both Leu43 and Leu77, which are solvent exposed and apparently separated from the central hydrophobic core. Helices 1, 2, and 4 pack around a central, predominantly hydrophobic cleft, with the more structured part of the first loop sitting at its base. The relative orientations of the aromatic groups Phe30, Phe35, and Tyr40 are well-defined in the base of the cleft, and the significant numbers of long-range NOEs to these residues (Figure 2) are responsible for defining the region of the loop.

Residues 19−29, though showing characteristic sequential NOEs, show no observable long-range NOEs and only a few short-range NOEs, mainly between Thr21 and Gly23. Structural definition of this region is therefore low. The CαH−NH(i,i + 2) contact between Thr21 and Gly23 is typical of a tight turn between residues Glu20 and Gly23. The structure over residues D22 and G23 is typical of a turn I′, but steric hindrance between T21 and D22 side chains prevents the full formation of the turn. No NH−NH(i,i + 2) was observed between Thr21 and Gly23, providing additional evidence that the tight turn has not fully formed.

(e) Buried Hydrophilic Groups. We reported previously (Crump et al., 1996) that Arg72 may be buried, because the large chemical shift difference (0.55 ppm) of the δCH protons suggested that the chain may be immobilized. Further analysis revealed additional weak NOEs between ζN protons and ϵN protons of Arg72 to both methyl groups of Leu31, confirming that it is buried. Similarly, the Cα and Cβ protons of Arg11 show long-range NOEs to the ring protons of the buried Phe30 residue, although in this case a large chemical shift difference is not observed for the side chain Cδ protons (0.07 ppm). Arg11 and Arg72 show fractional ASAs (Figure 4F) of 0.35 and 0.52 and $S(\chi^1)$ (Figure 4E) values of 1.00 and 0.99, respectively, suggesting that they are significantly immobilized and buried. On an atom-by-atom basis, the accessible areas of both Arg11 ζNH_2 groups are 36.7 and 38.3 Å^2 (evaluated with Chothia van der Waals radii), and both Arg72 ζNH_2 groups are 45.4 and 15.6 Å^2. These compare to a value of approximately 50 Å^2

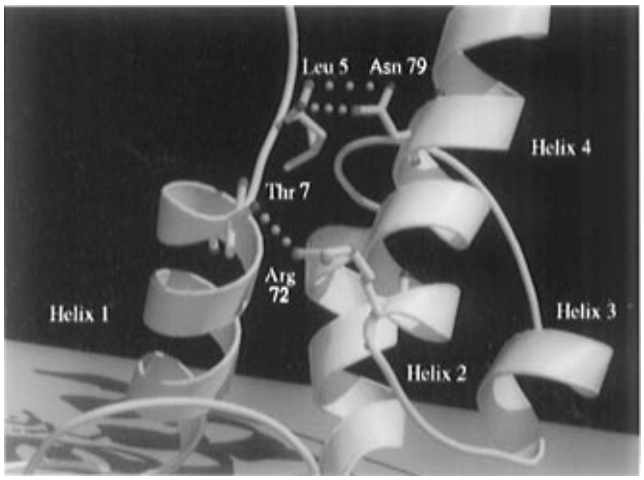

FIGURE 7: Schematic representation showing the partially buried Arg72 and Asn79 (100% conserved in all type II PKS ACPs) in the restrained minimized average structure of *act apo*-ACP. Putative hydrogen-bonding interactions are indicated for Thr7(γO) to Arg72(ζNH_2), Leu5(NH) to Asn79(γCO), and Leu5(CO) to Asn79(δNH_2). This figure was created using Molscript (Kraulis, 1991) and Raster3D (Merritt & Murphy, 1994).

for the same fully exposed groups in a model Gly-Arg-Gly tripeptide. Thus, in the average structure, the guanidinium group of Arg11 is solvent exposed while the hydrophobic region of the side chain is buried and packed against Phe30. Arg72 shows one well-buried ζNH_2 group with Thr7(γO) acting as a possible hydrogen bond acceptor for these protons (Figure 7). No restraint was explicitly included in the calculations for this interaction, and significant exchange broadening of the ζNH_2 resonances suggests that appreciable solvent exchange rates are still occurring. In addition, the ζNH_2 resonances are not observed during hydrogen-exchange experiments, suggesting that Arg72 may only be weakly hydrogen bonded.

Asn79 also appears to be buried in the final structures, showing a fractional ASA of 0.16 and an accessible area for the Nγ atom of only 10.9 Å^2 (approximately 35 Å^2 in a Gly-Asn-Gly tripeptide). The backbone amide of Leu5 shows slow amide exchange (protection factor >200), and clear NOE connectivities can be seen between the Asn γN protons and the Leu5 backbone amide proton. This brings the Asn(γNH_2) and Asn(γCO) groups in close proximity to the Leu5 backbone amide and carbonyl group, allowing the formation of Asn79(γNH_2)−Leu5(CO) and Leu5(NH)−Asn79(γCO) hydrogen bonds. Further evidence for burial of the Asn79 side chain comes from the observation of short-range NOEs from the γNH_2 group to the methyl groups of Leu75.

DISCUSSION

(a) Comparison of act apo-ACP with E. coli FAS ACP. The NMR structural studies have been centered solely on the *act apo*-ACP (Crosby et al., 1995), while previous NMR studies on *E. coli* FAS ACP have centered on the *holo* form. A NOESY spectrum collected on a *holo*/*apo* mixture (80%/20%) for *act* ACP was essentially unchanged when compared to the *apo* data (unpublished results). For *E. coli* ACP, 90% of the chemical shifts agreed to within 0.01 ppm when the *apo* and *holo* forms were compared (Andrec et al., 1995), and NOESY experiments suggested little interaction between the phosphopantetheine and ACP (Holak et al., 1988b). On this basis it also appears that little interaction occurs between the ACP and its phosphopantetheine cofactor in either the FAS or PKS proteins.

FIGURE 8: Best fit superposition of the minimized average structure of *act apo*-ACP (yellow) and the *E. coli* FAS ACP (purple). A single average model for *E. coli* ACP obtained from the Brookhaven Protein Data Bank was used for the fitting.

Comparison of the *E. coli* FAS ACP with the *act apo*-ACP indicates a common overall structure of an α-helical bundle. We recently showed that a strong secondary structure homology exists between *E. coli* FAS ACP and *act apo*-ACP, with the *act apo*-ACP having a very similar α-helical content (49%), compared with 51% in *E. coli* ACP (Crump et al., 1996). The solution structure of *E. coli* ACP (Holak et al., 1988a,b; Kim & Prestegard, 1990a) shows three helices (the fourth being short and not present in some models) arranged around a hydrophobic core which forms the presumptive binding site for a growing fatty acid chain (Jones et al., 1987). The structure is thought to be conformationally averaged between several states, perhaps reflecting flexibility required to accommodate a growing fatty acid chain (Kim & Prestegard, 1989). A superposition of the *act apo*-ACP on *E. coli* ACP over the backbone atoms of residues 5−18, 35−70, and 72−82 (*E. coli* ACP 3−16, 29−64, and 66−76) gives an RMSD of 2.4 Å (Figure 8), demonstrating that this homology extends to the solution structure. The well-structured part of the first loop separating helices 1 and 2 in *act apo*-ACP (30−41) shows some three-dimensional homology with the corresponding residues (24−35) in *E. coli* FAS ACP, while the preceding unstructured region, not surprisingly, shows larger differences. The unstructured portion of this loop in *act apo*-ACP contains three extra residues compared to *E. coli* ACP, and in both structures these residues are predominantly acidic and highly solvent exposed. Another structural difference is the disordered N-terminus (residues 2−3) in *act apo*-ACP followed by an extended structure over residues 4−6 preceding helix 1. This is significantly different from helix 1 in *E. coli* FAS ACP (helix 1, 3−15).

Important areas of homology exist around the almost 100% conserved D-S-L motif which is present at the N-terminus

of helix 2 in both *act apo*-ACP and *E. coli* ACP (Crump et al., 1996) and is preceded by several residues in the loop region with a similar tertiary fold. It has been shown that *E. coli holo*-synthase can phosphopantetheinylate *act apo*-ACP (at Ser42 within the motif) and also other PKS ACPs to significant degrees (Crosby et al., 1995). The ability of this FAS enzyme to recognize heterologous PKS ACPs suggests that the D-S-L motif forms an important molecular recognition site for the *holo*-synthase enzyme. None of the residues within this motif are significantly buried in the final average structure of *act apo*-ACP (frac surface accessibility >0.8), suggesting that they may all be available to form important interactions with the *holo*-synthase enzyme. Interestingly, a related PKS ACP from *Streptomyces griseus*, which has an E-S-L motif, was not modified to the *holo* form by *E. coli holo*-synthase, suggesting that a conservative mutation within this motif may prevent molecular recognition despite similar secondary structure in the *S. griseus* ACP (unpublished results).

The overall dynamics of *act apo*-ACP differ significantly from *E. coli* ACP. The structure of *act apo*-ACP has been determined with 699 experimental constraints of which 93 are long-range NOEs. In later calculations of the *E. coli* ACP structure (Kim & Prestegard, 1990a) 450 restraints with 48 long-range restraints were used. Neither *act apo*-ACP nor *E. coli* ACP benefits from the strong structure-stabilizing influence of intramolecular disulfide bridges, and as a result the proteins may be expected to adopt more flexible, open structures (Byeon & Llinás, 1991). Internal motion of the *E. coli* ACP around residues Phe50, Ile3, Leu45, and Ile72 led to the observation of abnormally short and variable distances between these residues and was the principal reason for invoking a conformationally averaged model. In *act apo*-ACP a homologous set of contacts are observed from Tyr56 (Leu5, Leu52, and Ile78), yet these long-range contacts are all satisfied in the final structures. Thus, despite a larger flexible loop and a slightly lower α-helical content (49% as opposed to 51%), *act apo*-ACP appears to show a single conformation on the NMR time scale as opposed to two or more states in the *E. coli* ACP. Although never structurally characterized, a similar interconversion of states for spinach ACP-I was observed (Kim & Prestegard, 1990b), suggesting that this phenomenon may be a general feature of FAS ACPs which is not present in PKS ACPs. The somewhat larger unstructured loop in *act apo*-ACP may therefore provide an alternate mechanism for allowing the ACP to accommodate a growing polyketide chain.

(b) Structure−Function of act ACP. The overall three-dimensional homology between *act apo*-ACP, *E. coli* FAS ACP, and other ACPs (Ghose et al., 1996) is strong, despite their differential roles. There is a general failure of FAS ACPs to substitute for PKS ACPs in genetically engineered systems [*E. coli* FAS ACP cannot substitute for *tcm* ACP (Shen & Hutchinson, 1993), *S. coelicolor's* own FAS ACP can substitute for *act* PKS ACP to only a very small extent (Revill et al., 1996), while the presumptive *Saccharopolyspora erythrea* FAS ACP (Hale et al., 1987) has only a low level of activity when substituted for *act* ACP (Khosla et al., 1992)]. This suggests that subtle differences may confer binding specificity to these proteins. *act apo*-ACP contains a number of buried polar groups in addition to the hydrophobic side chains expected to constitute a hydrophobic core. A polar environment and the presence of suitable hydrogen bond donors within the core of *act apo*-ACP may provide a mechanism for polyketide stabilization in a similar fashion to the stabilization of fatty acids within the hydrophobic cleft of FAS ACPs. Arginine side chains are commonly found in protein−protein/protein−ligand interactions (Mrabet et al., 1992). The guanidinium group of arginine may hydrogen bond to separate acceptors in a bidentate arrangement, or to just one acceptor, forming a bifurcated bond (Borders et al., 1994). Arg72 and Asn79, which are 100% conserved in the type II PKS ACPs, may be particularly important. We have observed NMR chemical shifts for the ϵNH of Arg73 and Arg71 (unpublished results) in *gris* and *otc* PKS ACPs, which are similar to that of *act* ACP (ϵNH 9.06 ppm) and similarly large splitting for the δCH_2 resonances. This suggests a conserved local structure surrounding this residue and permits the general observation that this group may always be partially buried. Attempts to identify a binding site for fatty acids in *E. coli* ACP (Jones et al., 1987) showed that residues at the N-terminus of helix 4 may be involved in interactions with the fatty acid. If a similar binding mode holds for polyketide ACPs, the Arg72 and Asn79 may be suitably positioned for interaction with the polyketide chain. Although the work of McDaniel et al. (1993a,b, 1994a,b, 1995a,b) has ruled against a programming role for the PKS ACPs, they may have an important stabilizing role for the elongated polyketide chain. In no case have partially assembled oligo−keto acid precursors of aromatic polyketides been isolated. This can, in part, be attributed to their inherent instability. Biomimetic studies (Harris & Harris, 1986) showed that under highly basic conditions pentamers or hexamers could be prepared by enolizing all the carbonyl groups, and it is clear that the compounds would spontaneously cyclize in neutral, aqueous solution. Cyclization of the polyketide chain has been shown to occur in a controlled fashion in aromatic polyketide biosynthesis, which suggests that important interactions between the polyketide chain and *act apo*-ACP may occur to sequester the chain from the aqueous environment and to stabilize the polyketide chain by hydrogen bonding, perhaps by enolizing several of the polyketide chain carbonyl groups. The lack of information on bound intermediates means that these interactions remain to be confirmed. It may be sufficient, however, to enolize just two of the eight carbonyl groups of actinorhodin (perhaps numbers three and six), leaving more stable diketide units. Since it has been shown that the minimal PKS and the next downstream enzyme, the ketoreductase, are required to control the initial cyclization (Fu et al., 1994b) (Figure 1), the bound polyketide may also form simultaneous noncovalent interactions with the ACP, ketosynthase, chain-length determining factor, and the ketoreductase. There is almost certainly the potential for enormous complexity in the interaction of the polyketides and the synthase subunits which may ensure high fidelity of polyketide processing. We are currently pursuing these ideas by investigating the precise interaction of the polyketide intermediates with the acyl carrier proteins and the isolation and characterization of the other components of the type II PKSs responsible for the biosynthesis of aromatic polyketides in streptomycetes.

ACKNOWLEDGMENT

We thank Nick Kelly for the kind gift of the specifically labeled leucine, Dr. Angelo Gargaro for technical discussions,

and Krishnakumar Rajarathnam for critical reading of the manuscript.

REFERENCES

Andrec, M., Hill, R. B., & Prestegard, J. H. (1995) *Protein Sci. 4*, 983−993.

Bai, Y., Milne, J. S., Mayne, L., & Englander, S. W. (1993) *Proteins: Struct., Funct., Genet. 17*, 75−86.

Bax, A., & Davis, D. G. (1985) *J. Magn. Reson. 65*, 355−360.

Borders, C. L., Broadwater, J. A., Bekeny, P. A., Salmon, J. E., Lee, A. S., Eldridge, A. M., & Pett, V. B. (1994) *Protein Sci. 3*, 541−548.

Braunschweiler, L., & Ernst, R. R. (1983) *J. Magn. Reson. 53*, 521−528.

Brünger, A. T., Kuriyan, J., & Karplus, M. (1987) *Science 235*, 458−460.

Byeon, I. L., & Llinás, M. (1991) *J. Mol. Biol. 222*, 1035−1051.

Crosby, J., Sherman, D. H., Bibb, M. J., Revill, W. P., Hopwood, D. A., & Simpson, T. J. (1995) *Biochim. Biophys. Acta 1251*, 32−42.

Crump, M. P., Crosby, J., Dempsey, C. E., Murray, M., Hopwood, D. A., & Simpson, T. J. (1996) *FEBS Lett. 391*, 302−306.

Fernández-Moreno, M. A., Martinez, E., Caballero, L., Ichinose, K., Hopwood, D. A., & Malpartida, F. (1994) *J. Biol. Chem. 269*, 24854−24863.

Fu, H., Ebert-Khosla, S., Hopwood, D. A., & Khosla, C. (1994a) *J. Am. Chem. Soc. 116*, 4166−4170.

Fu, H., Hopwood, D. A., & Khosla, C. (1994b) *Chem. Biol. 1*, 205−210.

Ghose, R., Geiger, O., & Prestegard, J. H. (1996) *FEBS Lett. 388*, 66−72.

Hale, R. S., Jordan, K. N., & Leadlay, P. F. (1987) *FEBS Lett. 224*, 133−136.

Hallam, S. E., Malpartida, F., & Hopwood, D. A. (1988) *Gene 74*, 305−320.

Harris, T. M., & Harris, C. M. (1986) *Pure Appl. Chem. 58*, 283−294.

Holak, T. A., Scarsdale, J. N., & Prestegard, J. H. (1987) *J. Magn. Reson. 74*, 546−549.

Holak, T. A., Engstrom, A., Kraulis, P. J., Lindeberg, G., Bennich, H., Jones, T. A., & Gronenborn, A. M. (1988a) *Biochemistry 27*, 7620−7629.

Holak, T. A., Nilges, M., Gronenborn, A. M., Clore, G. M., & Prestegard, J. H. (1988b) *Eur. J. Biochem. 175*, 9−15.

Hopwood, D. A., & Sherman, D. H. (1990) *Annu. Rev. Genet. 24*, 37−66.

Hopwood, D. A., & Khosla, C. (1992) in *Ciba Foundation Symposium*, No. 171, pp 88−112, Wiley, Chichester.

Hyberts, S. G., Goldberg, M. S., Havel., T. F., & Wagner, G. (1992) *Protein Sci. 1*, 736−751.

Jeener, J., Meier, B. H., Bachman, P., & Ernst, R. R. (1979) *J. Chem. Phys. 71*, 4546−4553.

Jones, P.-J., Holak, T. A., & Prestegard, J. H. (1987) *Biochemistry 26*, 3493−3500.

Kendrew, S. G., Harding, S. E., Hopwood, D. A., & Marsh, E. N. G. (1995) *J. Biol. Chem. 270*, 17339−17343.

Khosla, C., Ebert-Khosla, S., & Hopwood, D. A. (1992) *Mol. Microbiol. 6*, 3237−3249.

Khosla, C., McDaniel, R., Ebert-Khosla, S., Torres, R., Sherman, D. H., Bibb, M. J., & Hopwood, D. A. (1993) *J. Bacteriol. 175*, 2197−2204.

Kim, Y., & Prestegard, J. H. (1989) *Biochemistry 28*, 8792−8797.

Kim, Y., & Prestegard, J. H. (1990a) *Proteins: Struct., Funct., Genet. 8*, 377−385.

Kim, Y., & Prestegard, J. H. (1990b) *J. Am. Chem. Soc. 112*, 3707−3709.

Kraulis, P. J. (1991) *J. Appl. Crystallogr. 24*, 946−950.

Lee, B., & Richards, F. M. (1971) *J. Mol. Biol. 55*, 379−400.

MacArthur, M. W., & Thornton, J. M. (1993) *Proteins: Struct., Funct., Genet. 17*, 232−251.

McDaniel, R., Ebert-Khosla, S., Hopwood, D. A., & Khosla, C. (1993a) *Science 262*, 1546−1550.

McDaniel, R., Ebert-Khosla, S., Hopwood, D. A., & Khosla, C. (1993b) *J. Am. Chem. Soc. 115*, 11671−11675.

McDaniel, R., Ebert-Khosla, S., Hopwood, D. A., & Khosla, C. (1994a) *J. Am. Chem. Soc. 116*, 10855−10859.

McDaniel, R., Ebert-Khosla, S., Fu, H., Hopwood, D. A., & Khosla, C. (1994b) *Proc. Natl. Acad. Sci. U.S.A. 91*, 11542−11546.

McDaniel, R., Ebert-Khosla, S., Hopwood, D. A., & Khosla, C. (1995a) *Nature 375*, 549−554.

McDaniel, R., Hutchinson, C. R., & Khosla, C. (1995b) *J. Am. Chem. Soc. 117*, 6805−6810.

Merritt, E. A., & Murphy, M. E. P. (1994) *Acta Crystallogr. D50*, 869−873.

Morris, G. A., & Freeman, R. (1978) *J. Magn. Reson. 29*, 433−462.

Mrabet, N. T., Van der Broeck, A., Van den Brande, I., Stanssen, P., Laroche, Y., Lambeir, A., Matthijssens, G., Jenkins, J., Chiadmi, M., Van Tilbeurgh, H., Rey, F., Janin, J., Quax, W. J., Lasters, I., De Maeyer, M., & Wodak, S. J. (1992) *Biochemistry 31*, 2239−2252.

Mueller, L. (1987) *J. Magn. Reson. 72*, 191−196.

Nilges, M., Clore, G. M., & Gronenborn, A. M. (1988) *FEBS Lett. 239*, 129−136.

O'Hagan, D. (1991) *The Polyketide Metabolites*, Ellis Horwood, Chichester.

O'Hagan, D. (1995) *Nat. Prod. Rep. 12*, 1−32.

Pallaghy, P. K., Duggan, B. M., Pennington, M. W., & Norton, R. (1993) *J. Mol. Biol. 234*, 405−420.

Prescott, D. J., & Vagelos, P. R. (1972) *Adv. Enzymol. Relat. Areas Mol. Biol. 36*, 269−311.

Rance, M., Sørenson, O. W., Bodenhausen, G., Wagner, G., Ernst, R., & Wüthrich, K. (1983) *Biochem. Biophys. Res. Commun. 117*, 479−485.

Revill, W. P., Bibb, M. J., & Hopwood, D. A. (1996) *J. Bacteriol. 178*, 5660−5667.

Robinson, J. (1991) *Philos. Trans. R. Soc. London, B 332*, 107−114.

Ryckaert, J. P., Ciccotti, G., & Berendsen, H. J. C. (1977) *J. Comput. Phys. 23*, 327−341.

Shen, B., & Hutchinson, C. R. (1993) *Science 262*, 1535−1540.

Shen, B., Summers, R. G., Gramajo, H., Bibb, M. J., & Hutchinson, C. R. (1992) *J. Bacteriol. 174*, 3818−3821.

Simpson, T. J. (1995) *Chem. Ind. 11*, 407−411.

States, D. J., Haberhorn, R. A., & Ruben, D. J. (1982) *J. Magn. Reson. 48*, 286−292.

Wider, G., Macura, S., Kumar, A., Ernst, R. R., & Wüthrich, K. (1984) *J. Magn. Reson. 56*, 207−234.

Wüthrich, K., Billeter, M., & Braun, W. (1983) *J. Mol. Biol. 169*, 949−961.

BI970006+